# Deriving Mercury geodetic parameters with altimetric crossovers from the Mercury Laser Altimeter (MLA)

Stefano Bertone[1], Erwan Mazarico[2], Michael Barker[2], Sander Goossens[1], Terence Sabaka[2], Gregory Neumann[2], and David E Smith[3]

[1]University of Maryland Baltimore County
[2]NASA Goddard Space Flight Center
[3]Massachusetts Institute of Technology

November 24, 2022

**Abstract**

Based on previous applications of laser altimetry to planetary geodesy at GSFC, we use the recently developed PyXover software package to analyze altimetric crossovers from the Mercury Laser Altimeter (MLA). Using PyXover, we place new constraints on Mercury's geodetic parameters via least-squares minimization of crossover discrepancies. We simultaneously solve for orbital corrections for each MLA ground track, for the geodetic parameters of the IAU-recommended orientation model for Mercury (pole right-ascension and declination coordinates, prime meridian rotation rate and librations), and for the Mercury's Love number h2. We calibrate the formal errors of our solution based on closed-loop simulations and on the level of robustness against a priori values, data selection, and parametrization. Our solution of the Mercury's rotational parameters is consistent with published values. In particular, our new estimate for the orientation of the pole places Mercury in a Cassini state, with an obliquity = 2.031 $\pm$ 0.03 arcmin compatible with previous "surface" related measurements. Moreover, we provide a first data-based estimate of the Love number h2 = 1.55 +- 0.65. The latter is consistent with expectations from models of Mercury's interior, although its precision does not enable their refinement.

# Deriving Mercury geodetic parameters with altimetric crossovers from the Mercury Laser Altimeter (MLA)

**S. Bertone[1,2], E. Mazarico[2], M. K. Barker[2], S. Goossens[1,2], T. J. Sabaka[2], G. A. Neumann[2], and D. E. Smith[3,2]**

[1]Center for Research and Exploration in Space Science and Technology, University of Maryland Baltimore County, 1000 Hilltop Circle, Baltimore MD, USA
[2]NASA Goddard Space Flight Center (GSFC), 8800 Greenbelt Road, Greenbelt, MD 20771, USA
[3]Department of Earth, Atmospheric and Planetary Sciences, Massachusetts Institute of Technology, Cambridge, Massachusetts 02139, USA

**Key Points:**

- We provide an independent solution for Mercury's orientation parameters based on the analysis of the Mercury Laser Altimeter crossovers.
- Our solution places Mercury in a Cassini state with an obliquity $\epsilon = 2.03 \pm 0.03$, larger than the recent gravity-based estimate.
- We provide a first constraint on Mercury's tidal Love number $h_2$ to be in the range from 0.9 to 2.2.

Corresponding author: Stefano Bertone, `stefano.bertone@nasa.gov`

## Abstract

Based on previous applications of laser altimetry to planetary geodesy at GSFC, we use the recently developed PyXover software package to analyze altimetric crossovers from the Mercury Laser Altimeter (MLA). Using PyXover, we place new constraints on Mercury's geodetic parameters via least-squares minimization of crossover discrepancies. We simultaneously solve for orbital corrections for each MLA ground track, for the geodetic parameters of the IAU-recommended orientation model for Mercury (pole right-ascension and declination coordinates, prime meridian rotation rate and librations), and for the Mercury's Love number $h_2$. We calibrate the formal errors of our solution based on closed-loop simulations and on the level of robustness against a priori values, data selection, and parametrization. Our solution of the Mercury's rotational parameters is consistent with published values. In particular, our new estimate for the orientation of the pole places Mercury in a Cassini state, with an obliquity $\epsilon = 2.031\pm0.03$ arcmin compatible with previous "surface" related measurements. Moreover, we provide a first data-based estimate of the Love number $h_2 = 1.55\pm0.65$. The latter is consistent with expectations from models of Mercury's interior, although its precision does not enable their refinement.


## Plain Language Summary

Measuring the orientation of bodies in space is one of the few means we have to learn about their internal structure. We analyze Mercury's orientation from distance measurements between the planet's surface and the MESSENGER probe, acquired with laser pulses from orbit around Mercury between 2011 and 2015. In particular, we use observations of the same surface locations at different times, called crossovers. Any difference in the measured elevation at these crossover points results either from an error in MESSENGER's estimated position in space or from an error in the assumed orientation of Mercury. Based on these differences, we make corrections to both MESSENGER's trajectory and to the pole position, rotation rate and oscillations of Mercury. Tides raised on Mercury by the Sun are also expected to periodically vary the surface elevation by more than 2 meters. Since these tidal effects are also expressed as elevation differences at the crossovers, our analysis provides a first measurement of their amplitude. Our updates to Mercury's orientation and tidal response bring important information about its internal structure, such as the size of its core and its internal level of differentiation.

## 1 Introduction

Mercury is one of the most interesting objects in the Solar System, still challenging our understanding of planetary formation and evolution with its high density, unexpected magnetic field, and the $3:2$ resonance between its rotational and orbital periods.

After the early flybys by Mariner 10 in the 1970s, the MESSENGER spacecraft (MErcury Surface, Space ENvironment, GEochemistry, and Ranging; Solomon et al., 2008) executed three equatorial flybys of Mercury in $2008-2009$ before entering a highly elliptical, near-polar orbit from March 2011 to April 2015. Mercury's orientation and rotation have been studied by a variety of techniques, as they have implications for the moment of inertia of the outer solid shell and thus its mass distribution, internal structure, and thermal evolution of Mercury (*e.g.*, Margot et al., 2012; Phillips et al., 2018; Genova et al., 2019). Already before MESSENGER, Margot (2009) used ground-based radar observations to develop early orientation models. Several independent confirmations and refinements of Mercury's rotational parameters followed, based on a variety of techniques using multiple MESSENGER datasets. In particular, Mazarico et al. (2014), Verma and Margot (2016), Genova et al. (2019), and Konopliv et al. (2020) all analyzed the radio tracking data of the MESSENGER spacecraft, with different approaches; Stark et al. (2015) co-registered altimetry from the Mercury Laser Altimeter (MLA, Cavanaugh et al., 2007) and shape models derived from the Mercury Dual Imaging System (MDIS) camera images. Solutions for most rotational parameters agree within provided error bars (with a wide range of magnitudes), yet significant differences are present between recent estimates of both the orientation of the pole and Mercury's spin rate.

While several orbit determination (OD) based studies have provided estimates of Mercury's tidal Love number $k_2$ (Mazarico et al., 2014; Verma & Margot, 2016; Genova et al., 2019), no data-based solution for the vertical Love number $h_2$ has been produced to date, mainly because of the small expected signal (a maximum vertical deformation of $< 2.5$ meters at the equator and 50 cm at the poles for $h_2 = 1$), because of the poor knowledge of small scale topography required to use direct altimetry analysis (Thor et al., 2020), and because of MESSENGER's orbital configuration, which strongly limits the density of altimetry crossovers at latitudes $< 30°N$.

MLA collected measurements of surface height during $\sim 3,200$ periapsis passes over Mercury's northern hemisphere. Where two MLA groundtracks intersect, we get a so-called crossover point. A crossover is thus a differential measurement between two distinct observations of the same surface location at two different times. Any difference in height at the crossover point, referred to as its discrepancy $v$, is thus mainly due to the following effects: (1) errors in the spacecraft orbit and attitude, or small variations (due to thermal deformations or other environmental conditions) to MLA fixed boresight orientation, (2) interpolation errors of the surface topography between MLA footprints, and (3) geophysical signal, *e.g.*, due to mismodeled time-varying planetary rotation or to tidal vertical motions. Although crossovers require a complex processing pipeline, they are a powerful tool to explore the state of planetary bodies (Rowlands et al., 1999; Rosat et al., 2008; Mazarico et al., 2014) and provide an opportunity to measure Mercury's orientation and rotation. In our study, we provide an independent solution based on the application of this technique to MLA crossovers with the in-house PyXover code (Bertone et al., 2020), that we recently developed for this analysis. The resulting discrepancies $v$ constitute the observation residuals to be minimized in the least-squares (LS) procedure, involving the simultaneous adjustments of MESSENGER orbit corrections and Mercury's geodetic parameters. Within an iterative procedure, we solve for four of the orientation parameters of the model recommended by the International Astronomical Union (IAU, Archinal et al., 2018), *i.e.*, right ascension (RA) and declination (DEC) of the spin pole at $J2000$, spin rate ($\omega$), and a scale factor for the librations amplitude (L) of Mercury, as well as for the degree-2 tidal radial response $h_2$.

This paper is structured as follows. In section 2, we present our reference dataset and the auxiliary data used for this study. Details about the data weighting and solution strategy are provided in section 3. Finally, our solution and error calibration for Mercury's orientation and tidal parameters based on MLA crossover analysis are presented in section 4 and discussed in section 5. Throughout the text, we use small bold letters to denote vector quantities, and capital bold letters for matrices.

## 2 Data description, modeling and parametrization

The MESSENGER spacecraft orbited Mercury between 2011 and 2015 in a highly-elliptical, near-polar orbit with a periapsis of $\sim 200-400$ km, an apoapsis between $\sim 15000-20000$ km, and an orbital period of 12 hrs initially and reduced to 8 hrs after

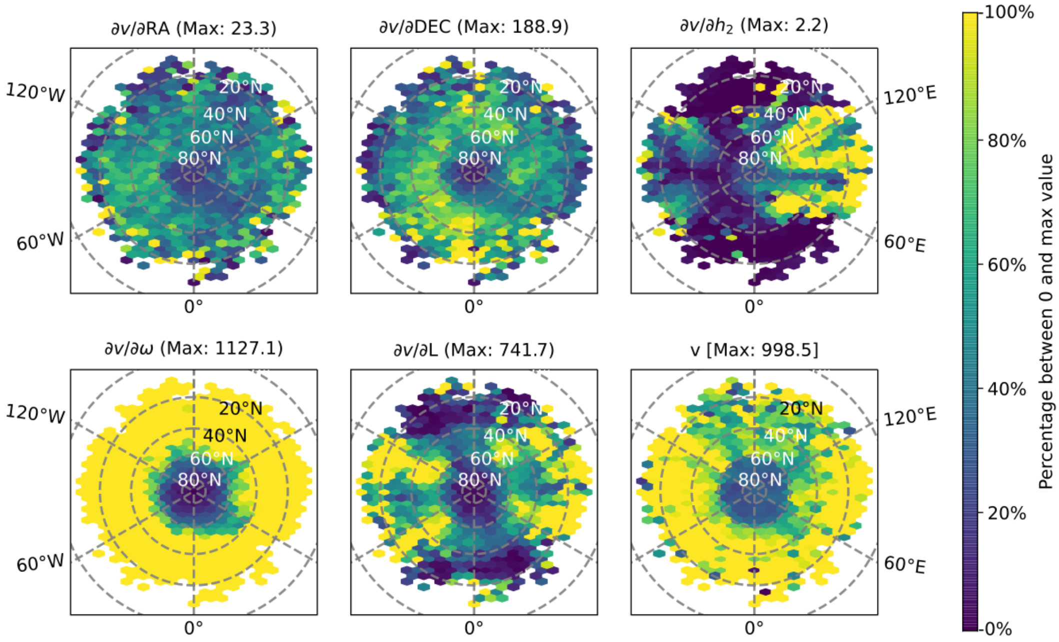


**Figure 1.** North-polar stereographic map of MLA crossovers sensitivity to several rotational and tidal Mercury's parameters. Bottom-right: pre-fit crossovers discrepancies $v$ on Mercury surface.

one year. The spacecraft was within ranging distance for the onboard MLA instrument over 15-45 min periods near periapsis, typically at Northern latitudes. MLA collected over 22 million measurements of surface height with a vertical precision of $\sim 1$ m and an accuracy of $\sim 10$ m (Zuber et al., 2012).

Because of the elliptical orbit, the laser spot diameter on the surface varies between $\sim 10 - 100$ m. The inter-spot distance is then $\sim 350 - 450$ m, so that the average distance between each crossover and its bracketing spots is usually $\sim 200$ m (Zuber et al., 2012). The total MLA dataset contains $\sim 3,200$ tracks and $\sim 3$ million crossovers, geographically distributed as shown in Fig. 1 (bottom-right). These crossovers represent repeated measurements of the same surface locations, such that any difference between the elevation measured along the two profiles results from an error either in the orbit and attitude reconstruction, or in the a priori knowledge of the planetary rotation and tidal response. Fig. 1 shows the partial derivatives of MLA crossovers, and hence their sensitivity to the parameters of interest as a function of their geographical location on the surface of Mercury.

From the MLA dataset available on the NASA Planetary Data System, we extract the laser pulse emission time in Barycentric Dynamical Time (TDB, Soffel et al., 2003) and the Time of Flight (TOF) of the signal, along with the *channel* associated with each measurement. Data with a "channel" value $> 4$ include an elevated level of noise and are thus excluded from our analysis. If multiple data points within the nominal 10 Hz sampling rate are available, we only include the one with the lowest channel value, *i.e.*, the most reliable.

Our processing, detailed in section 3, also requires a reference orbit and attitude for the spacecraft carrying the altimeter. We mostly refer to the MESSENGER orbits reconstructed by KinetX based on radio tracking by the Deep Space Network (DSN) antennas and on the spacecraft attitude provided by on-board star-trackers. Both are available as NAIF/Spice (Acton et al., 2018) kernels on the NASA PDS, where the telemetered attitude has already been corrected for aberration effects. We process these kernels via the SpiceyPy wrapper for Python (Annex et al., 2020). In section 4.4, we also perform our analysis on MESSENGER orbits based on the Genova et al. (2019) processing baseline, in order to quantify the independence of our solution from a priori orbits and to a more robust estimate.

We model the resulting crossover discrepancies $v$ as a function of errors in the a priori orbit, as well as of deviations from the IAU rotational model (Archinal et al., 2018) and as mismodeling of tidal deformations. These constitute our estimated parameters vector $\boldsymbol{q}$. Orbital parameters include corrections to the a priori orbit which can be modeled as a constant offset estimated once for each track in every direction of the orbital frame: along-track $A$, cross-track $C$, and radial $R$. In addition, attitude (roll and pitch) biases and time-dependent corrections (*e.g.*, linear or quadratic) could be estimated for each track within PyXover, but we do not want to over-parametrize our solution. Additional geodetic parameters characterize the tidal deformation of Mercury and its orientation in space, and enter the geolocation of the MLA groundtracks via the transformation from the inertial frame (in which the MESSENGER orbits are provided) to the Mercury-fixed frame (where MLA groundtracks need to be rotated to form crossovers). Following the IAU formalism (Archinal et al., 2018), we parameterize the orientation of Mercury by the right ascension (RA or $\alpha$) and declination (DEC or $\delta$) of Mercury's pole at J2000 (their secular trends are fixed to their nominal IAU values). The planetary prime meridian (PM) direction is also modeled as a quadratic function of time (since J2000).

In the following, we indicate by $\omega$ and estimate exclusively the linear term of this series, *i.e.*, the spin rate. On top of this, we consider the longitudinal libration (L), *i.e.* the sum of all the terms at different periods from Margot (2009). We then estimate corrections to the pole orientation at J2000, to Mercury's spin rate, and a scaling factor $(1+\frac{dL}{L})$ for Mercury's librations.

To model the solid tidal displacement $u_r$ at Mercury surface, we use a solid tide model based on the degree 2 potential terms exerted by the Sun (*e.g.*, Van Hoolst & Jacobs, 2003), so that

$$u_r(\boldsymbol{r}, t) = -\frac{h_2 V_2(\boldsymbol{r}, t)}{g} \,, \tag{1}$$

where $h_2$ is the Love number of degree 2, $g$ is the gravitational acceleration at the surface, and

$$V_2(\boldsymbol{r}, t) = -\frac{GM}{2}\frac{r^2}{R^3}(3\cos^2\psi - 1) \tag{2}$$

is the tidal potential caused by the Sun at a point on Mercury surface with coordinates $\boldsymbol{r}$, with $G$ the universal gravity constant, $M$ the mass of the Sun, $R$ the distance between the centers of mass of the Sun and Mercury, and $\psi$ the angle between the Mercury-centric directions of the Sun and of the point considered.

## 3 Processing and solution strategy

We perform the analysis of MLA crossovers within the recently developed PyXover python package (Bertone et al., 2020), whose modular structure is sketched in Fig. 2.

The crossover analysis can be divided into three main steps. First, laser altimetry ranges are geolocated to the planetary surface (*i.e.*, we assign a set of latitude, longitude and elevation in the planet frame to each MLA shot) and partial derivatives of the groundtracks are computed with the chosen set of parameters $\boldsymbol{q}$ by finite differencing. Initial geolocation is based on a set of reference orbit solutions for MESSENGER (see section 4) and on a priori knowledge of Mercury's orientation (*e.g.*, Archinal et al., 2018). Tidal deformations are modeled according to Van Hoolst and Jacobs (2003) with the a priori value for $h_2$ set to 0.

Second, intersections between the tracks are identified and characterized. The horizontal coordinates $(\bar{x}_0, \bar{y}_0)$ of the crossover points are first computed in a local North polar stereographic projection, to provide an approximate location of all possible intersections. For computational reasons, the tracks are sub-sampled to a ratio of $1:4$, that is, looking for intersections between straight lines connecting MLA measurements $\sim 1200$ meters from each other. This (time consuming) step is performed only once to locate the horizontal coordinates of potential crossovers. Subsequent iterations only refine crossover coordinates based on results from previous iterations. Short track segments constituted of the (fully sampled) 4 MLA observations involved in a potential crossover are thus analyzed. We reproject the coordinates of each subtrack around the preliminary crossover coordinates and fine-tune them. To finally compute the elevation discrepancy

$$v = \eta_A - \eta_B \ , \tag{3}$$

for all confirmed crossovers, we interpolate MLA-derived elevations along each track $A$ and $B$ using cubic splines to determine elevations $\eta_A$ and $\eta_B$ at the refined crossover coordinates $(x_0, y_0)$. The discrepancies vector $\boldsymbol{v}$ constitutes the residuals to be minimized in the LS optimization process. Moreover, we associate each measurement $v$ with a weight according to its reliability, following criteria detailed in section 3.2.

The corrections $\boldsymbol{\delta q}$ resulting from the LS inversion detailed in section 3.3 are then applied to parameters values from previous iteration $\boldsymbol{q}_i$, so that $\boldsymbol{q}_{i+1} = \boldsymbol{q}_i + \boldsymbol{\delta q}$. Updated orbits and geodetic parameters constitute the basis for the following iteration, including a new geolocation of the MLA data, the fine determination of new crossovers tridimensional coordinates and of a new residual vector $\boldsymbol{v}$ and of the associated partial derivatives. We set the following criteria for convergence: first, when the Root Mean Square Error (RMSE) of residuals stabilizes within 5%, we fix the weighting of observations to the latest evaluation and we start estimating $h_2$, which is initially held fixed to 0 because of its correlation with orbital errors; then, we further iterate with fixed observation weights until the relative improvement of residuals RMSE falls below 1% and corrections for global parameters are lower than their formal errors at $3\sigma$. This usually happens within $< 10$ iterations. The choice of different convergence criteria would impact the rate of convergence rather than the final solution.

### 3.1 Computation of the crossover partial derivatives

From Eq. (3), we obtain the partial derivatives of each discrepancy $v$ at intersection of tracks $A$ and $B$ with respect to a parameter $q$ belonging to $\boldsymbol{q}$ as

$$\frac{dv}{dq} = \frac{d\eta_A}{dq} - \frac{d\eta_B}{dq} \ . \tag{4}$$

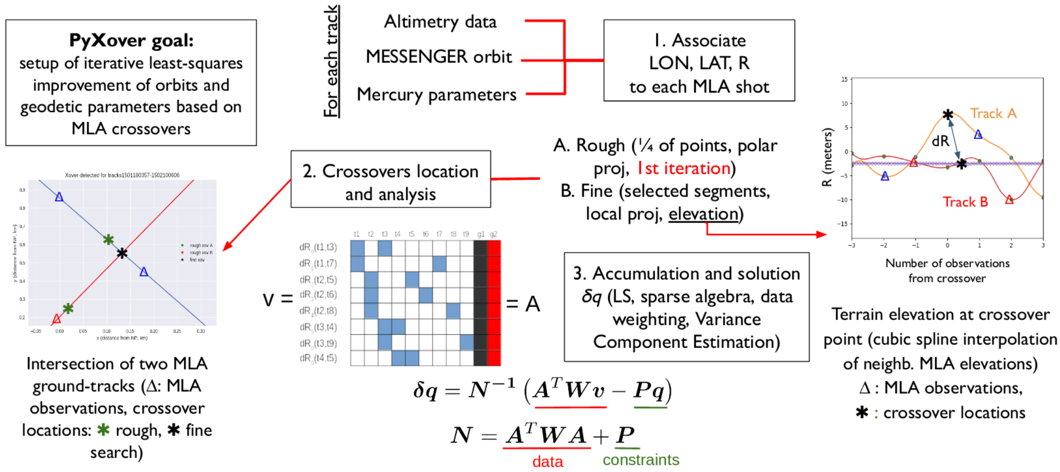


**Figure 2.** Workflow of the PyXover code: geolocation of altimetry data, crossovers location and setup of observation equations, QR-filter solution for a chosen set of parameters, with given weights and constraints.

By expanding Eq. (3), we also obtain

$$v(\eta_A, \eta_B) = v\left[\eta_A(\lambda_A, \phi_A, \boldsymbol{q}), \eta_B(\lambda_B, \phi_B, \boldsymbol{q})\right] \ , \tag{5}$$

with $\lambda_X$ the longitude, $\phi_X$ the co-latitude, and $\eta_X$ the elevation of a measurement from track $X$, while $\boldsymbol{q}$ is the vector of the solved-for orbital and geodetic parameters, so that

$$\frac{d\eta}{dq} = \frac{\partial \eta}{\partial \lambda}\frac{\partial \lambda}{\partial q} + \frac{\partial \eta}{\partial \phi}\frac{\partial \phi}{\partial q} + \frac{\partial \eta}{\partial q} \ . \tag{6}$$

During the geolocation phase, we compute the partial derivatives $\frac{\partial \lambda}{\partial q}, \frac{\partial \phi}{\partial q}$, and $\frac{\partial \eta}{\partial q}$ numerically, by finite differencing of the ground location of individual MLA shots. Derivatives with respect to $h_2$ are an exception. Indeed, based on Eq. (1), and considering that $\eta(\boldsymbol{r}, t) = \eta_0(\boldsymbol{r}) + u_r(\boldsymbol{r}, t)$, the analytical expression of $\frac{\partial \eta}{\partial h_2}$ is straightforward. We also obtain updated epochs for the intersection of the laser pulses with the surface for tracks perturbed with respect to each parameter, in order to compute the accurate planetary state at bounce. We get "perturbed groundtracks" $(\lambda, \phi)_q$ by linear extrapolation as

$$(\lambda, \phi)_q = (\lambda, \phi)_0 \pm (\frac{\partial \lambda}{\partial q}, \frac{\partial \phi}{\partial q})\Delta q \tag{7}$$

from the nominal groundtrack $(\lambda, \phi)_0$ using an appropriate increment $\Delta q$. Based on these perturbed tracks, we locate perturbed crossover coordinates and further correct the elevation by $\frac{\partial \eta}{\partial q}$. For each track $X$, we finally compute Eq. (6) numerically by

$$\frac{d\eta_X}{dq} = \frac{\eta_X(q_+) - \eta_X(q_-)}{2\Delta q} \ , \tag{8}$$

where $\pm$ indicate the elevation at crossover points of "positively and negatively" perturbed tracks. We are then able to fully compute Eq. (4) and thus populate the partials (or first design) matrix $\mathbf{A}$.

### 3.2 Data weighting

The quality of the crossovers included in the analysis can affect the estimation of our results. Instead of removing poor pseudo-measurements, we associate a weight to each crossover based on several factors determining its reliability: belonging to a "well behaved" MLA track, being close to neighboring MLA measurements, belonging to close-to-nadir measurements, and not having an unreasonably large a priori discrepancy. This helps the stability of the LS solution by maintaining a uniform dataset among iterations.

First, we evaluate the quality of OD for each MLA track involved in our analysis. For each of the $N_\tau = 3200$ tracks, we analyze the residuals of all $N_w(i_\tau)$ crossovers resulting from intersections of track $i_\tau$ with the remaining tracks over the whole MESSENGER mission. The average bias of the resulting time series (preemptively screened for large outliers) enable the evaluation of the quality of each track. Fig. 3 shows examples of a "good" track (left), where the rather noisy residuals are centered around 0, and of a "bad" track (right), where residuals are globally biased. The resulting error $\sigma_\tau$ associated to each track is then propagated to a full covariance matrix at the crossover level, by setting

$$\boldsymbol{\Sigma_{w\tau}} = \boldsymbol{A_\tau \Sigma_\tau A_\tau^T} \, , \tag{9}$$

where $\boldsymbol{\Sigma_\tau}$ is a $(N_\tau \times N_\tau)$ covariance matrix containing $\sigma_\tau$ for each track on the main diagonal and zeros elsewhere, while $\boldsymbol{A_\tau}$ is the $(N_w \times N_\tau)$ transfer matrix between tracks and crossovers, where for each observation column $j$, $\boldsymbol{A_{\tau j}} = \pm 1$ if the track $\tau_j$ intervenes in the crossover, else $\boldsymbol{A_{\tau j}} = 0$. We obtain the related weight matrix by taking the element-wise inverse of $\boldsymbol{\Sigma_{w\tau}}$. The resulting weight matrix is clearly non diagonal. This procedure identifies and down-weights crossovers carrying erroneous information from one of the parent tracks. As shown in Fig. 3 (right), an unreliable track also includes crossovers with $v \sim 0$, which could degrade the solution if included in the analysis by a less sophisticated screening.

The second main source of error in $v$ is the interpolation noise. The use of altimetry crossovers considerably reduces the reliance of our analysis on the Digital Terrain Model

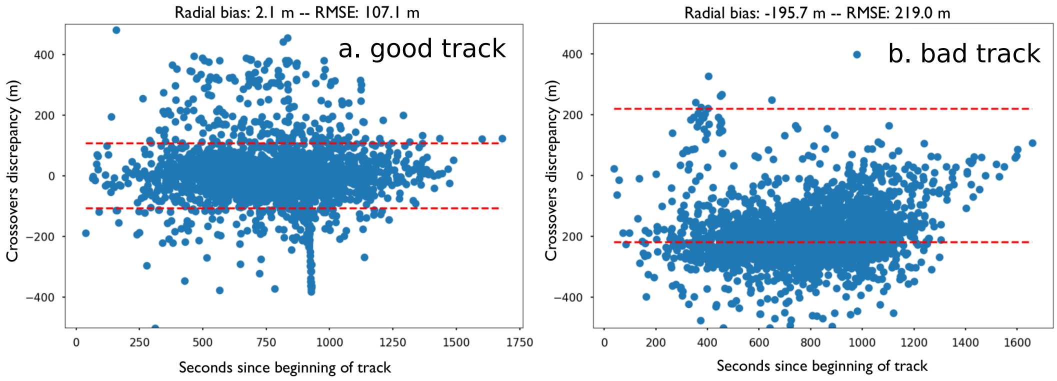


**Figure 3.** Examples of good (a) and bad (b) tracks (RMSE in meters vs. time in seconds along the track, red dashed lines at ± RMSE). Using this criterion, also crossovers with $v \sim 0$ from (b) will be significantly down-weighted.

(DTM) quality. Still, because of the finite MLA sampling of 10 Hz and the high orbital velocity of the spacecraft around periapsis ($\sim 4.3$ km/s), chances that the crossover location coincides with an altimetric measurement are low. Because of the limited knowledge of Mercury topography at baselines relevant for our analysis (*i.e.*, from the 20 meters laser footprint to the 400 meters of average separation, see Zuber et al., 2012), we use a cubic spline to interpolate elevation profiles from the bracketing track points to the crossover location. This operation introduces an additional error $\sigma_{w\iota}$, which in principle depends on both the separation and the terrain roughness (*i.e.*, the interpolation error will be lower on a smooth plain than in a rough area). In this study, however, we use an average terrain roughness of 100 m/km$^2$ based on Kreslavsky et al. (2014), as detailed roughness maps are not available at latitudes $< 65°$ N. For each crossover, we compute the average of the minimal separation of each profile and use it as reference baseline for the observation. We extrapolate the regional roughness at this baseline using the spectral power of Mercury's surface as derived from the stereo DTM data provided by Steinbrügge et al. (2018). We consider this roughness at separation as an indicator of the relative interpolation error $\sigma_{w\iota}$ between crossovers, and the associated weight matrix to have a value of $1/\sigma_{w\iota}$ on the main diagonal.

On top of this, Huber weighting (defined as $wt = (\bar{k}/k)^q$ if $k > \bar{k}$, $wt = 1$ otherwise) is then applied to each crossover according to its off-nadir angle ($\bar{k} = 2°$, $q = 1$), while crossovers with abnormally large residuals ($v > 50$ meters, $q = 1$) are strongly down-weighted.

All weight components are then multiplied for each crossover observation to get the final weight matrix $\mathbf{W}$ to be associated with residuals $\boldsymbol{v}$ and partial derivatives in $\mathbf{A}$ used in computing the LS solution.

### 3.3 Solution strategy

Given the partial derivatives in $\mathbf{A}$, we estimate corrections $\boldsymbol{\delta q}$ to the parameter vector $\boldsymbol{q}$ by minimizing the RMSE of the measurement residuals vector $\boldsymbol{v}$ so that

$$\boldsymbol{\delta q} = \left(\boldsymbol{A}^T\boldsymbol{W}\boldsymbol{A} + \boldsymbol{P}\right)^{-1}\left[\boldsymbol{A}^T\boldsymbol{W}\boldsymbol{v} - \boldsymbol{P}(\boldsymbol{q} - \boldsymbol{q_0})\right] \ , \tag{10}$$

where values for all quantities have to be intended at iteration $i$, except for $\boldsymbol{q}_0$ indicating the a priori value of the estimated parameters.

Weak constraints $\mathbf{P}$ are applied, mainly to contain the impact of correlations between orbit and geodetic parameters. We use ridge regression (Tikhonov et al., 1998) to penalize statistically large variations for orbit parameters and deviations of the average orbital corrections in each direction (from an expectation of 0). This helps improve correlations between, *e.g.*, an offset in the determination of the spin and a solid rotation of all (quasi-)polar MESSENGER orbits in the cross-track direction. We use Variance Component Estimation (VCE, Kusche, 2003) to determine the optimal weights between observations and constraints and to both stabilize the solution and get more realistic error estimates. Following Lemoine et al. (2013), we define the VCE determined weight $\lambda^{VCE} \equiv \sigma_{VCE}^{-2}$ by

$$\sigma_{VCE}^2 = \sigma_0^2\left[\frac{(\boldsymbol{v} - \mathbf{A}\delta q)^T\mathbf{W}(\boldsymbol{v} - \mathbf{A}\delta q)}{N - Tr(\mathbf{A}^T\mathbf{W}\mathbf{A}\mathbf{N}^{-1})}\right] \ . \tag{11}$$

for observations and

$$\sigma_{VCE}^2 = \sigma_0^2\left[\frac{\boldsymbol{q}^T\mathbf{P}\boldsymbol{q}}{N - Tr(\mathbf{P}\mathbf{N}^{-1})}\right] \ . \tag{12}$$

for constraints, and with the constrained normal matrix $\mathbf{N} = \mathbf{A}^T\mathbf{W}\mathbf{A} + \mathbf{P}$. In particular, we compute two separate weights for parameter constraints and for constraints acting on average values of orbit corrections, so that

$$\mathbf{P} = \boldsymbol{\Lambda}_{\bar{q}}\mathbf{P}_{\bar{q}} + \boldsymbol{\Lambda}_q\mathbf{P}_q \ , \tag{13}$$

where $\boldsymbol{\Lambda}$ is a diagonal matrix having as elements

$$\Lambda = \lambda^{VCE}\boldsymbol{\lambda} \ , \tag{14}$$

$\boldsymbol{\lambda}$ is a vector the size of $\boldsymbol{q}$, manually set to constrain parameters with respect to each other (based on the reliability of prior knowledge and on preliminary simulations), $\boldsymbol{P}_q$ is a diagonal square matrix with the size of the total number of parameters and values 0 or 1, depending on the corresponding parameter in the solution vector $p$, and

$$\mathbf{P}_{\bar{q}} = (\mathbb{I} - \frac{\mathbb{1}\mathbb{1}^T}{N}) \,, \tag{15}$$

with $\mathbb{I}$ the identity and $\mathbb{1}$ the unary matrix, respectively. This procedure stabilizes our solution, by providing an optimal balance between amplitude of the solution vector $\boldsymbol{\delta q}$ and the minimization of the residuals vector $\boldsymbol{v}$.

By introducing the Cholesky square root of $\mathbf{P}$ on both sides of the observation equations, we finally set-up the Square Root Information Filter (SRIF, Bierman, 1977) solution algorithm, as depicted in Fig. 2. Given the size of the $\mathbf{A}$ matrix (*i.e.*, up to $3\times 10^6$ observations/rows per $\sim 8000$ parameters/columns) and its low density, we use sparse algebra operations provided by the SciPy library (Virtanen et al., 2020) to efficiently perform the required matrix manipulations.

## 4 Iterative solution and error assessment

We perform an iterative weighted LS solution of orbit corrections and geodetic parameters based on the processing setup presented in section 3. We base our solution on a set of $10^6$ crossovers selected according to their computed weight (*i.e.*, their quality) and to their balanced geographical distribution. The quality threshold is thus higher above $60°N$ latitude, while at low latitudes only the worst 20% of the crossovers are excluded, given the latter are more sensitive to parameters of interest. We show in Fig. 4 the distribution of the weights as a function of discrepancies $v$ and of the separation to the bracketing points.

We use KinetX-recovered MESSENGER orbits and the IAU orientation models (Archinal et al., 2018) recommended for Mercury as a priori. Following the procedure sketched in section 3, we estimate corrections for orbit and geodetic parameters until convergence is reached (see Fig. 5). Typical orbital corrections are in the order of $50-100$ meters for "per-track" biases in along- and cross-track directions and 20 meters in the radial direction, as shown in Fig. 6.

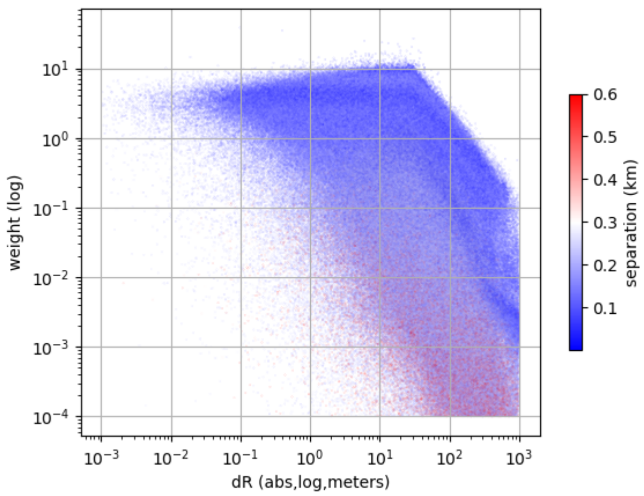


**Figure 4.** Log-log representation of the weights assigned to each crossover point as function of its discrepancy. The color scale shows the average minimal separation between the crossover and the neighboring observations. Huber weighting ensures a sharp cutoff for crossovers with $v > 100$ meters. One can see that small values of $v$ do not ensure a high weight. Also, most observations with high separation show large residuals and low weights.

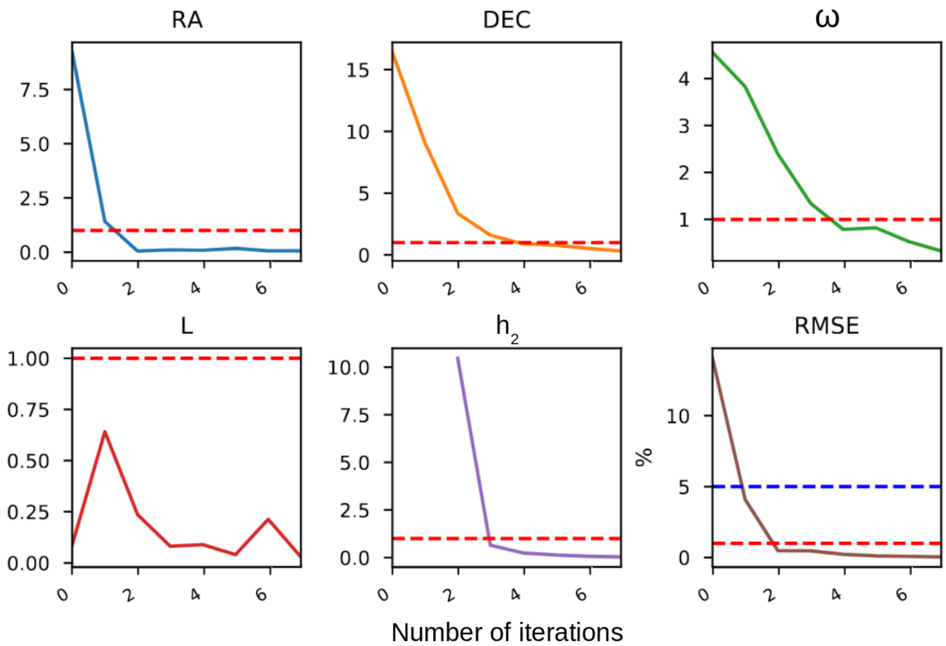


**Figure 5.** Convergence of residuals RMSE and geodetic parameter corrections for a reference iterated solution. The y-scales indicate, for each iteration, the parameter improvements in units of the associated formal errors (red, $3\sigma$) and, bottom-right, the percentage RMSE change (blue-red dashed lines at $5\% - 1\%$, respectively)

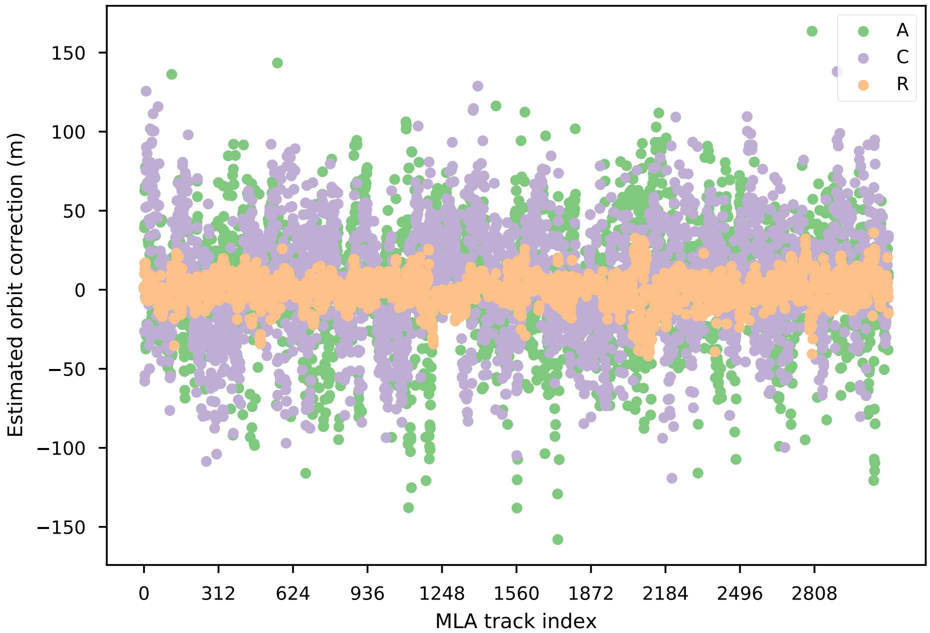


**Figure 6.** Orbit corrections at convergence, parametrized as biases in MESSENGER orbital frame (radial, along-, and cross-track) estimated for each MLA track (*i.e.*, once per orbit). Larger corrections in the along- and cross-track indicate a lower sensitivity of both radio-science and crossovers to these components. A few larger outliers up to several hundred meters have been removed to enhance visualisation.

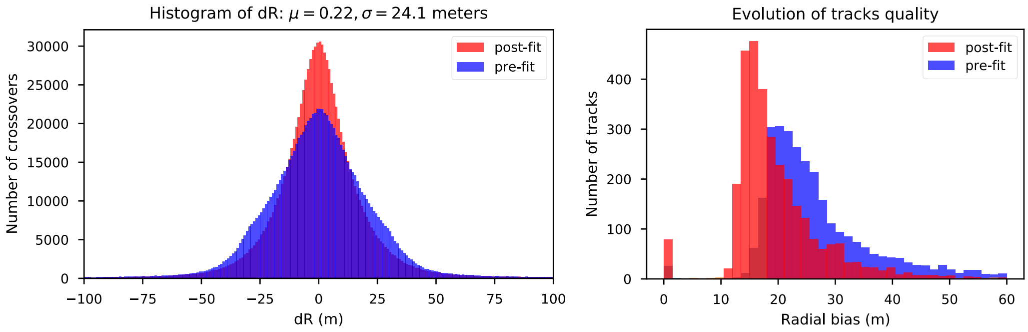


**Figure 7.** Pre- (FWHM=35 meters) and post-fit (FWHM=24 meters) assessment of discrepancies residuals (left) and improvement in the distribution of tracks quality, evaluated by the average bias of their crossovers (right)

In order to assess the quality of the obtained solution, we check several factors. As shown in Fig. 7, the distribution and RMSE of post-fit crossover discrepancies significantly improves, as expected. Also, we check that individual MESSENGER tracks benefit from our estimated corrections, by comparing pre- and post-fit distributions. Our iterated solution results in significant improvements on the base of all the above criteria.

Formal errors resulting from LS and VCE notoriously neglect systematic errors intervening in the solution. In sections 4.1 to 4.4 we thus analyze several possible sources of systematic errors, *i.e.*, the a priori chosen for MESSENGER trajectory and the Mercury's rotational state, data selection and other intrinsic biases in our crossover analysis (which we evaluate by processing a simulated MLA dataset). The resulting error budget is summarized in Table 1, while our final solution including calibrated error bars is shown in Fig. 11. Correlations between these parameters are $< 0.3$ when using the whole MLA crossovers dataset, while only $\sim 3\%$ of all orbit parameters have correlations $> 0.9$, mainly between along-track and radial corrections estimated for the same track.

### 4.1 Influence of a priori MESSENGER orbit and rotational parameters

We compute solutions based on different Doppler orbit reconstructions (KinetX and Genova et al., 2018) and from both IAU (Archinal et al., 2018) and Genova et al. (2019) values for Mercury's rotational parameters. We analyze the 4 possible combinations and

| Parameter | solution | formal | systematic | a priori | subset | intrinsic |
|---|---|---|---|---|---|---|
| RA (°) | 281.0093 | $5.4 \times 10^{-5}$ | $5.8 \times 10^{-4}$ | $5.3 \times 10^{-4}$ | $5. \times 10^{-5}$ | $1.5 \times 10^{-5}$ |
| DEC (°) | 61.4153 | $2.8 \times 10^{-5}$ | $4.6 \times 10^{-4}$ | $3.8 \times 10^{-4}$ | $8.5 \times 10^{-5}$ | $7 \times 10^{-6}$ |
| $\omega$ (°/$d$) | 6.138510 | $1.5 \times 10^{-7}$ | $2.7 \times 10^{-6}$ | $2.7 \times 10^{-6}$ | $4. \times 10^{-8}$ | $8. \times 10^{-8}$ |
| L (as) | 39.03 | 0.2 | 0.9 | 0.7 | 0.15 | 0.04 |
| $h_2$ | 1.55 | 0.3 | 0.35 | 0.2 | 0.08 | 0.1 |

**Table 1.** Summary of solutions, statistical and systematic sources of error for our crossovers analysis. Least-squares provided formal errors are scaled by a factor 3 to provide a more robust range of parameter values, while the “systematic” column is the sum of: influence of a priori values, data selection, and other intrinsic biases in our analysis.

compare parameter solutions at convergence in Fig. 8. Clustering is visible for most solutions. The solution shown in Table 1 and in Fig. 11 is the weighted average of these solutions according to their respective formal errors. We use the statistical dispersion of these solutions to evaluate the systematic error introduced by the choice of a priori values and to update formal error bars, as summarized in column “a priori” of Table 1.

Orbits derived from Genova et al. (2019) show a lower consistency with MLA crossovers than KinetX orbits, possibly due to the chosen minimal parametrization with empirical terms. Hence, we first estimate a priori offsets for the spacecraft positions to get a refined a priori geolocated track for the iterative crossover analysis. In particular, we use the quasi-Newton Broyden-Fletcher-Goldfarb-Shanno (BFGS) numerical optimization method (Jorge Nocedal, 2006) to minimize differences of MLA measured elevations to Mercury’s DTM, which reduces crossover residuals to a level close to the one obtained from KinetX orbits.

### 4.2 Influence of data sampling

To analyze the impact of data sampling on our solution, we construct 10 different random subsets of $5{\times}10^5$ crossovers out of the full MLA dataset (after removing 10% of data with the lowest quality). We choose a stratified resampling without replacement, in order to retain the latitudinal distribution of the original dataset. Common data among

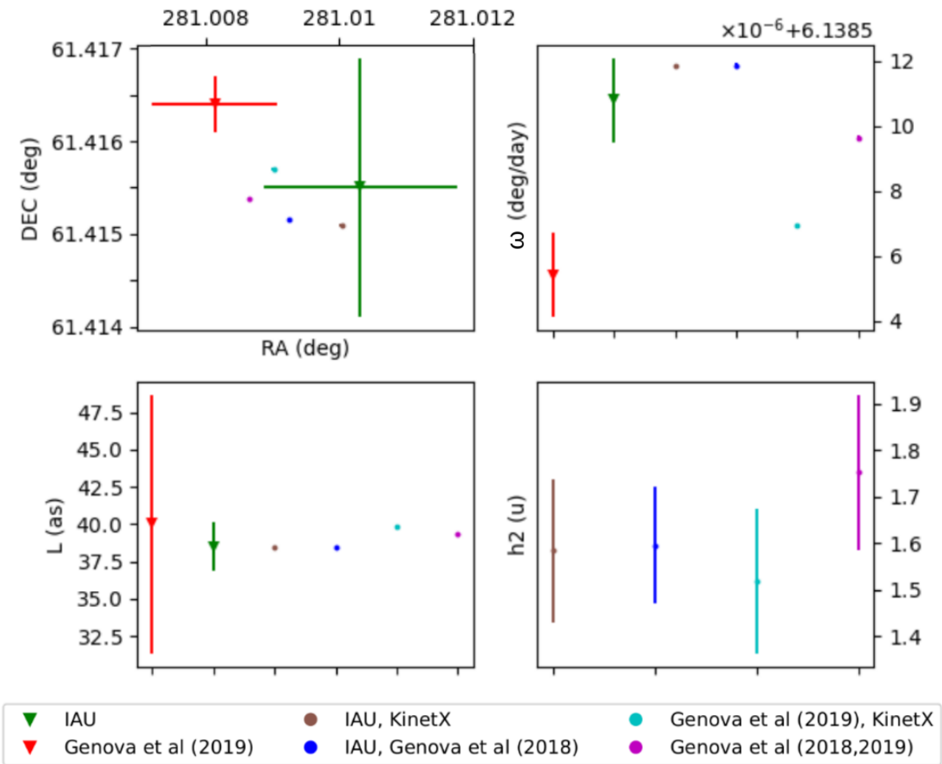


**Figure 8.** Comparison of our solutions for [RA, DEC, $\omega$, L, $h_2$], based on a set of $10^6$ crossovers, and using the same parametrization and data selection criteria, but on different combinations of MESSENGER orbit reconstructions (KinetX and Genova et al., 2018) and rotational parameters, *i.e.*, IAU, Archinal et al. (2018) and Genova et al. (2019), as a priori values (green and red triangles). The dispersion of the converged solutions (colored dots) is used to evaluate the systematic error introduced by the choice of a priori.

any pair of subsets do not exceed 20%. We compute a fully iterated solution for each subset and measure their dispersion.

The dispersion of most solutions falls well within the formal error bars provided by the LS (the dispersion of $L$ and $h_2$ are comparable with formal error bars), and we conclude that our solution is robust with respect to an arbitrary selection of MLA measurements and resulting crossovers. Statistical results of this analysis are summarized in column "subset" of Table 1.

### 4.3 Influence of orbit constraints

As discussed in Section 3.3, we apply VCE to identify optimal relative weights for data (*i.e.*, crossovers discrepancies) and parameter constraints. We get $\lambda_{\bar{q}}^{VCE} = 10$ and $\lambda_{q}^{VCE} = 1$ relative to the unweighted data. By choice, constraints are only acting on orbital ACR corrections (full value and average over the whole mission), while geodetic parameters are freely estimated.

We found that constraint $\lambda_{\bar{q}}^{VCE}$, acting on the global average of estimated ACR corrections (which is expected to be close to 0 as the a priori dynamic solution is known to be unbiased on the whole), is the main factor to consider and explored the impact of a wide range of values. Fig. 9 shows the variation of the global 3-dimensional mean (green) and RMS (red) of orbital corrections over the whole mission, as a function of $\lambda_{\bar{q}}^{VCE}$ and of the crossovers RMSE. As expected, the crossover fits (x-axis) degrade with tighter constraints. Different mean values correspond to a global shift of ACR corrections, rather than to isolated outliers (as verified with median values and visual inspection). We use this representation to perform an L-curve analysis (Hansen, 1999) based on the (green) means vs crossovers RMSE curve, and get a weight $\lambda_{\bar{q}}^{VCE} = 5$, close to the one suggested by VCE. The total RMS of corrections (red) shows the orbit variations allowed by our current parametrization and weighting, consistently with Fig. 6.

Concerning our solution for Mercury's orientation and tidal parameters, we only found a significant impact on the estimate of $h_2$, while estimates for other parameters are stable within their error bars. Fig. 9 (bottom) illustrates the range of possible $h_2$ estimates for a set of (IAU, KinetX)-based solutions only differing by $\lambda_{\bar{q}}^{VCE}$. We highlight in grey the range of "optimal estimates" favored by VCE and L-curve analysis. The average value of this range, together with formal and systematic errors shown in Table 1,

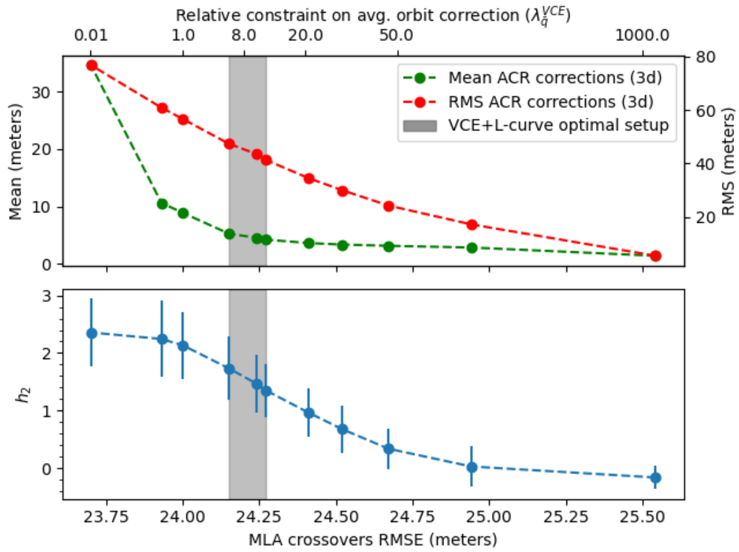


**Figure 9.** Influence of the relative weighting of data and constraints on estimated orbit corrections (top) and tidal parameter $h_2$ (bottom). Each point corresponds to the solution of a subset of 500,000 crossover discrepancies with different constraint applied on the averages of ACR orbit corrections computed over the whole mission. Resulting averages of 3D corrections (green) are used to validate the VCE-based weighting via an L-curve analysis; the resulting total RMS (red) of corrections is also shown for reference. Relative constraints favored by VCE and L-curve (grey area indicating $5 < \lambda_{\bar{q}}^{VCE} < 10$) also define a range of favored $h_2$ values.

result in a best estimate of $h_2 = 1.55 \pm 0.65$. Solutions based on Genova et al. (2019) a priori orbits generally require a stronger orbit regularization to converge on consistent results.

### 4.4 Validation on simulated data

To fully characterize the behavior of the solutions, and in order to choose an appropriate parametrization and weighting scheme, we conduct extensive simulations with time-of-flight ranges consistently generated from a realistic topography.

To model small scale Mercury topography, we compute a fractal noise map composed by 5 superposed levels: the main noise level has an amplitude of 30 meters on a 600 meters baseline, while for each of the following ones the amplitude is divided by $\sqrt{2}$ and the baseline is halved, consistently with the structure function of Mercury topography estimated by, *e.g.* Susorney et al. (2017) and Steinbrügge et al. (2018). Instead of a map for the full surface, we generate a limited size "stamp" (Mazarico et al., 2015) of $0.25° \times 0.25°$ with a periodic pattern in both latitude and longitude, such as the one shown in Fig. 10. For each set of coordinates on Mercury surface, we define the local elevation as the sum of MLA derived topography and of the simulated small-scale noise.

We simulate the full MLA dataset and repeat the selection procedure outlined in section 4 to select the "best" $10^6$ crossovers. We first check the impact of the interpolation error on crossovers residuals and on the recovery of the geodetic parameters, by considering a perfect knowledge of MESSENGER trajectory and Mercury's orientation and tides. We show the distribution of the resulting discrepancies (FWMH $<$ 10 meters) in Fig. 10, while estimated parameter corrections (expected to be 0) have amplitudes of $10^{-5}$ deg for RA, $10^{-6}$ deg for DEC, $5.\times10^{-9}$ deg/day for $\omega$, $10^{-3}$ arcsec for L, and 0.075 for $h_2$.

Then, we analyze a more realistic situation, where both the orbits and the geodetic parameters are perturbed. To simulate a realistic mismodeling occurring in the processing of real data, we degrade our a priori knowledge by applying both a bias and linear drift in ACR and a bias to pointing parameters, but only estimate a set of ACR biases per each track. Perturbations have been set to an RMSE of 50 meters (+40 meters/day) in AC and 20 meters (+10 meters/day) in R, 0.5 arcsec for the pointing, 5 arcsec for right-ascension and declination of the pole, 3 as/y for the spin rate, and 1.5 arcsec for libra-

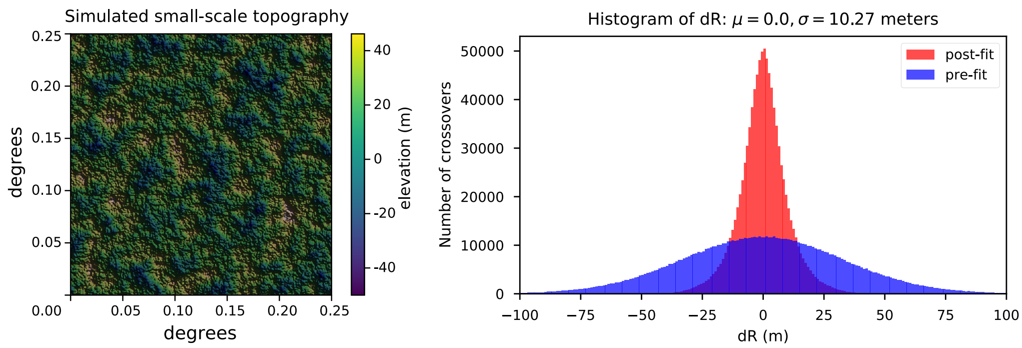


**Figure 10.** Left: Simulated small-scale topography of Mercury surface. Right: Crossover discrepancies histogram (meters) of perturbed simulation setup (blue) and “zero-test” (only including interpolation noise, red).

tions, according to the value of current uncertitudes (Archinal et al., 2018). Orbit and pointing perturbations are randomly chosen for each track, according to the selected RMSE. An histogram of discrepancies for each experiment is shown in Fig. 10: pre-fit discrepancies of the perturbed solution are comparable with the ones of real MLA data. We report in Table 1 (column “intrinsic”) the parameter residuals at convergence, *i.e.* the difference between the applied perturbations and the solution. We consider these as intrinsic errors from the processing pipeline (*e.g.*, interpolation noise, numerical errors, and imperfections in our modeling and parametrization), also contributing to the systematic errors budget of our analysis.

## 5 Discussion

Our solution for the Mercury’s rotational parameters, based on the full MLA dataset and an average of solutions with different a priori orbits and values (see section 4.1), is shown in Fig. 11 along with previous solutions provided by other groups using various techniques (camera and altimetry, Doppler, Earth-based radar). Our updated values and calibrated error bars (based on the analysis presented in section 4) are consistent with most recent solutions and provide an independent validation.

Our solution puts Mercury in a precise Cassini state, as predicted by dynamical models (Peale, 1988), without any explicit constraints to place it in this state. While deviations from the Cassini state of the order of a few arc-seconds are expected (*e.g.*, due

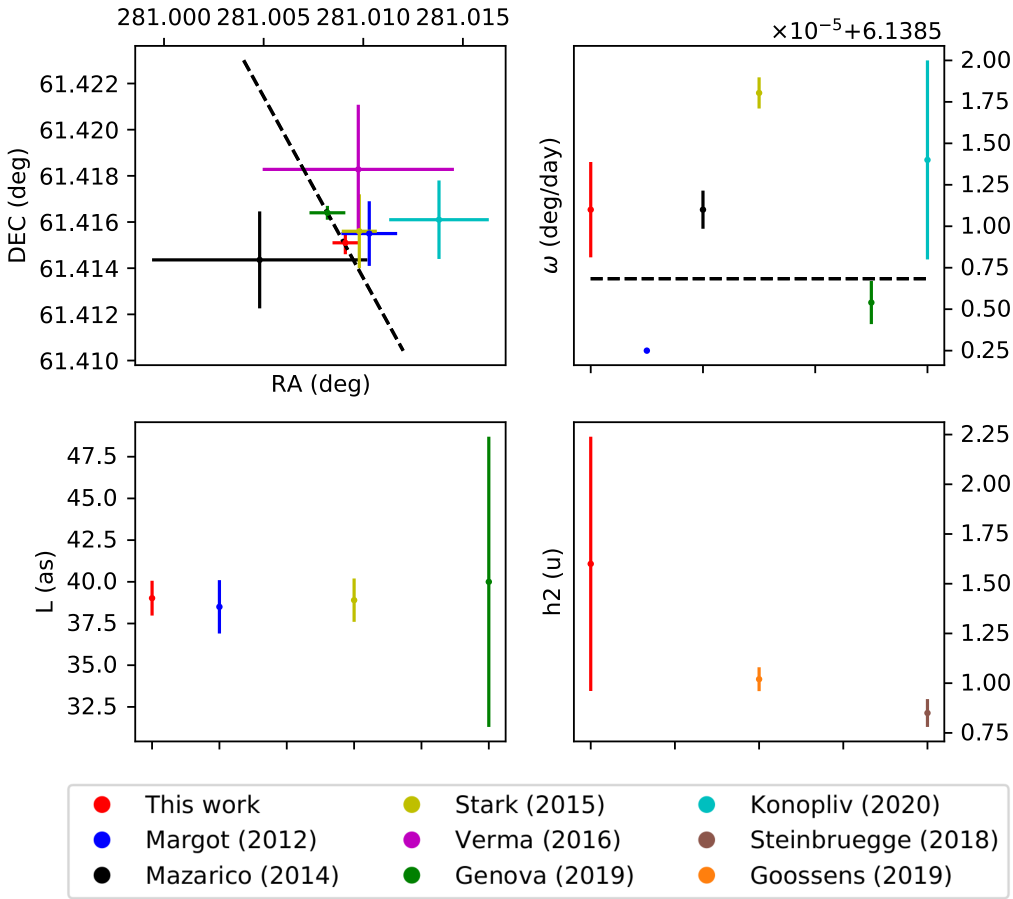


**Figure 11.** Our solutions for Mercury's orientation (RA, DEC, $\omega$, L) and tidal Love number $h_2$ based on MLA crossovers analysis (red, $3\sigma$ errors), compared with Margot (2009) (blue), Mazarico et al. (2014) (black), Stark et al. (2015) (yellow), Verma and Margot (2016) (mauve), Genova et al. (2019) (green), and Konopliv et al. (2020) (cyan), all using different datasets and techniques. As ours is the first data-based estimate of Mercury's $h_2$, we compare our solution to theoretical predictions from Steinbrügge et al. (2018) (brown) and Goossens et al. (2019) (orange). Black dashed lines indicate either the Cassini plane (RA/DEC) or Mercury's resonant spin rate ($\omega$).

| | RA (°) | DEC (°) | $\omega$ (°/day) | L (m) | $\epsilon$ (arcmin) | $C/MR^2$ |
|---|---|---|---|---|---|---|
| Margot (2009) | $\mathbf{281.0103 \pm 1.4 \times 10^{-3}}$ | $\mathbf{61.4155 \pm 1.4 \times 10^{-3}}$ | 6.1385025 | $\mathbf{38.5 \pm 1.6}$ | $2.04 \pm 0.08$ | $0.346 \pm 0.014$ |
| Mazarico et al. (2014) | $281.00480 \pm 0.0054$ | $61.41436 \pm 0.0021$ | $\mathbf{6.138511 \pm 1.15 \times 10^{-6}}$ | - | $2.06 \pm 0.16$ | $0.349 \pm 0.014$ |
| Stark et al. (2015) | $281.00980 \pm 8.8 \times 10^{-4}$ | $61.4156 \pm 1.6 \times 10^{-3}$ | $6.13851804 \pm 9.4 \times 10^{-7}$ | $38.9 \pm 1.3$ | $2.029 \pm 0.085$ | $0.3437 \pm 0.011$ |
| Verma and Margot (2016) | $281.00975 \pm 4.8 \times 10^{-3}$ | $61.41828 \pm 2.8 \times 10^{-3}$ | - | - | $1.88 \pm 0.16$ | $0.318 \pm 0.028$ |
| Genova et al. (2019) | $281.0082 \pm 9.4 \times 10^{-4}$ | $61.4164 \pm 3. \times 10^{-4}$ | $6.1385054 \pm 1.3 \times 10^{-6}$ | $40.0 \pm 8.7$ | $1.968 \pm 0.027$ | $0.333 \pm 0.005$ |
| Konopliv et al. (2020)† | $281.0138 \pm 2.5 \times 10^{-3}$ | $61.4161 \pm 1.7 \times 10^{-3}$ | $6.138514 \pm 6 \times 10^{-6}$ | - | $2.04 \pm 0.12$† | $0.345 \pm 0.020$† |
| This study | $281.0093 \pm 6.3 \times 10^{-4}$ | $61.4153 \pm 4.8 \times 10^{-4}$ | $6.138510 \pm 2.8 \times 10^{-6}$ | $39.03 \pm 1.1$ | $2.031 \pm 0.03$ | $0.343 \pm 0.006$ |

**Table 2.** Values of Mercury's orientation parameters, $\epsilon$, and $C/MR^2$: updated version based on Baland et al. (2017). In bold the values currently adopted by the IAU (Archinal et al., 2018). † The obliquity $\epsilon$ given by Konopliv et al. (2020) is inconsistent with the pole axis orientation they report, as already noted by Steinbrügge et al. (2020): we derived values for $\epsilon$ and $C/MR^2$.

to the precession of perihelion or to tidal dissipation, see Baland et al., 2017), these are of the order of our error bars and significantly smaller than offsets presented by most previous solutions (also see, e.g., Dumberry, 2020). Compared to the gravity measurements provided by Genova et al. (2019) (also in agreement with a Cassini state), we get a higher obliquity $\epsilon = 2.031 \pm 0.03$ arcmin, consistent with a normalized polar moment of inertia $C/MR^2 = 0.343 \pm 0.006$ (with $C$, $M$, and $R$ the polar moment of inertia, mass, and radius of Mercury, respectively). Explicit equations for these quantities are given in Genova et al. (2019) (supplementary material, where we note that Eq.5 contains a typo and should read

$$\epsilon = \frac{\frac{C}{MR^2}\dot{\Omega}\sin i}{\frac{C}{MR^2}\dot{\Omega}\cos i + 2n\boldsymbol{G_{210}}(e)C_{22} - n\boldsymbol{G_{201}}(e)C_{20}}$$

) , while Baland et al. (2017) provides useful numerical values and a detailed discussion of the underlying dynamical theory. Recent estimates for Mercury's rotational parameters, obliquity and polar moment of inertia (and associated errors) are summarized and compared in Table 2, updating a similar table from Baland et al. (2017). Our crossover-based solution is hence closer to previous estimates from Earth-based radar (Margot et al., 2012) and from imagery and altimetry (Stark et al., 2015), but with smaller error bars. Since these techniques are tied to and sensitive to the rotation of the crust only, while gravity measurements by Verma and Margot (2016) and Genova et al. (2019) sense the whole planet, the discrepancy between these values might be interpreted as a different state for different layers of the planet. Geophysical implications of our results are presented later in this section.

Concerning Mercury's spin rate, our solution favors Mazarico et al. (2014), rather than the other analysis which used MLA data (Stark et al., 2015). Error bars values in Table 1 are the result of a thorough evaluation (*e.g.*, already reflect the sensitivity of the solution to a priori values and parametrization) and can thus be used as such. Regarding the amplitude of Mercury's longitudinal librations, our solution is consistent with the literature, with error bars comparable with previous "surface measurements" by Margot et al. (2012) and Stark et al. (2015). Based on the polar moment of inertia and estimate for longitudinal librations, we compute the ratio $C_{cr+m}/C = 0.423 \pm 0.012$, where $C_{cr+m}$ is the fractional polar moment of inertia of the solid crust plus mantle and values $\sim 0.5$ indicate a fluid outer core.

We then use a Markov Chain Monte Carlo (MCMC) process to generate an ensemble of interior models of Mercury. Our models follow earlier works: pressure variations with depth are computed using hydrostatic assumptions, and we numerically integrate the differential equations for pressure, gravity, and temperature (Sohl & Spohn, 1997; Hauck et al., 2013; Knibbe & van Westrenen, 2015). Based on these values, we determine the local density from equations of state. Our approach is entirely based on our earlier work as reported in Genova et al. (2019) (using the same parameters for the equations of state). We use our newly derived values for $C/MR^2$ and $C_{cr+m}/C$ as measurements, together with a constraint of 0.2% on the bulk density of Mercury (the same as in Genova et al, 2019). Our MCMC results thus satisfy Mercury's mass constraint. As was the case before, the outer core radius is the parameter that is best determined (Hauck et al., 2013; Genova et al., 2019). As shown in Fig. 12, our best estimate for the outer core radius $r_{oc} = 2020 \pm 50$ km (at $3\sigma$) is significantly larger than what estimated in gravity analysis by Genova et al. (2019), but close to the value estimated by Hauck et al. (2013). Because our polar moment value is close to that used by the latter, our MCMC results are also very similar. This is the case for the outer core radius, but also for other parameters such as the mantle density and weight fraction of Si in the core (not shown here). An important difference with the results used in Hauck et al. (2013), however, is that our rotation state is exactly in the Cassini state. This allows us to directly apply the procedure outlined by Peale et al. (2002) to derive Mercury's internal structure from our estimates. In addition, our error bars are smaller, which results in smaller error bars on the outer core radius. Because our polar moment value is larger than that of Genova et al. (2019), our outer core radius is also larger. Because the estimate of Genova et al.

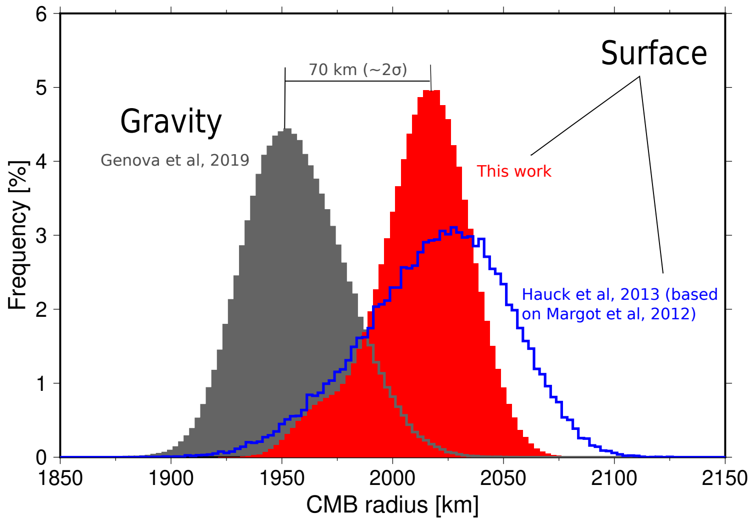


**Figure 12.** Outer core radius, $r_{oc}$, resulting from Markov chain Monte Carlo solutions consistent with values of Mercury's moment of inertia $C/MR^2$ and $C_{cr+m}/C$ based on our analysis of MLA altimetry crossovers. As for previous solutions based on the tracking of surface features, our best estimate for $r_{oc}$ is significantly larger than gravity estimates by Genova et al. (2019) (also shown, for comparison).

(2019) was based on gravity, indicating a sensitivity to the whole planet, and ours on measurements related to the crust, this further illustrates a possible difference between these measurements. While it is unclear which measurement type (if any) would yield the correct answer on its own, one has to be aware of these differences, because they have consequences for the resolved interior models: a higher polar moment as resolved from crustal measurements results in a larger outer core radius, and might not be able to constrain a solid inner core (Hauck et al., 2013; Margot et al., 2018). We note the latter in our results as well. Despite a smaller error, our current MCMC results do not make a distinction between the solid and liquid core as we find that their density is often close to one another.

As differential measurements of Mercury's surface elevation, altimetry crossovers are sensitive to vertical displacements due to the tidal influence of other bodies (mainly the Sun), and hence to the Love number $h_2$. However, the geographical distribution of MLA crossovers and of tidal deformations at Mercury surface (see Fig. 13), along with their amplitude ($>2$ meters only at limited longitudes and close to Mercury equator)

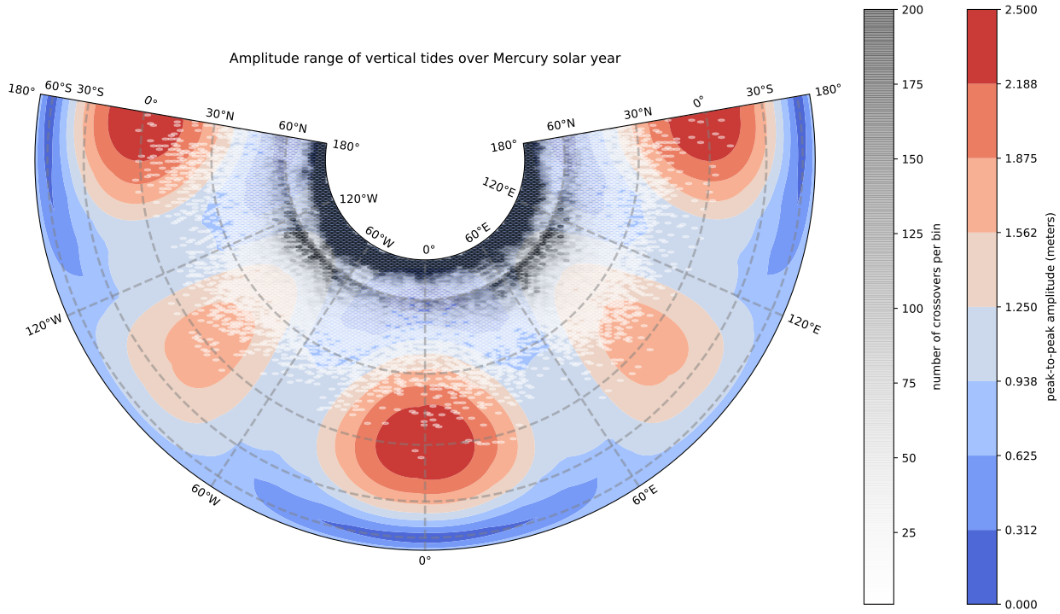


**Figure 13.** The geographical distribution of MLA crossovers (darker areas indicate more crossovers per sq. km) is superposed to a map of the total Mercury's tidal deformations (for $h_2 = 1$) integrated over a Mercury year. The comparison shows that although most MLA crossovers lie in regions where deformations are below 1 meter, a large variety of tidal patterns are covered.

makes tidal variations particularly challenging to measure with currently available measurements from orbit.

When combined with measurements of the gravitational Love number $k_2$, $h_2$ provides important constraints on the deep interior of a body, such as its inner core size (Van Hoolst & Jacobs, 2003; Steinbrügge et al., 2018). Up to now, the value of Mercury's $h_2$ has only been predicted based on Mercury's mean density and moment of inertia inferred from the MESSENGER mission data analysis ($0.77 < h_2 < 0.93$, Steinbrügge et al., 2018, based on $C/MR^2 = 0.34$ and $k_2 = 0.46$) and on Markov-Chain Monte-Carlo (MCMC) analysis of Mercury's interior taking into account experimental measurements of its moment of inertia and gravitational tidal response ($h_2 = 1.02 \pm 0.06$, by Goossens et al., 2019, based on estimates by Genova et al., 2019).

In section 4 we provided our solution for $h_2$ and highlighted how its estimate from MLA data is a delicate matter, sensitive to orbital errors and to the choice of constraints and parametrization. We discussed in Sec. 4.3 how to partially mitigate these factors,

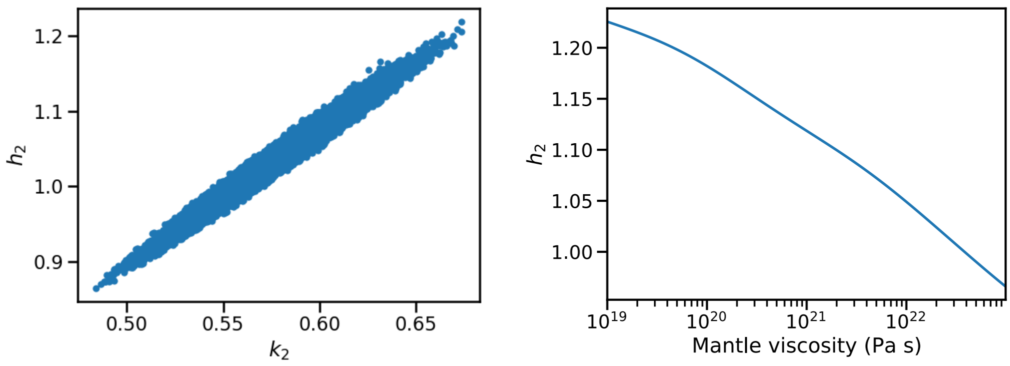


**Figure 14.** $h_2$ and $k_2$ have a positive correlation when using current reference values in simulations of Mercury interior: results from the MCMC analysis shown in Fig. 12 indicate that $h_2 < 1.1$ is expected given current $k_2$ estimates (**left**). However, this behaviour is sensitive to a multitude of model parameters such as mantle viscosity (**right**) or the rheology model (here we adopt Andrade rheology, see Andrade, 1910; Jackson, 1993). For these reasons we opt not to force our $h_2$ solution to be close to model predictions.

and set our error bars accordingly. Our error budget includes the main error sources identified in previous studies (*e.g.*, elevation interpolation, orbital and pointing errors, see Steinbrügge et al., 2018) but also systematic errors due to sampling, LS constraints, and the choice of a priori orbits and rotational parameters. Fig. 14 shows that larger $h_2$ values would correspond to larger $k_2$ values, according to MCMC-derived correlations. As such, only the lower part of our solution range for $h_2 = 1.55 \pm 0.65$ would map on current best estimates of $k_2$ by Genova et al, 2019 at $3\sigma$ level. We could in principle apply tighter constraints towards 0 on either our $h_2$ estimate or MESSENGER orbit corrections to "regularise" our solution towards values closer to the "expected" $h_2 \sim 1$, but we rather choose to provide a loosely constrained solution. While the upper and central part of our solution range is hardly compatible with, e.g., recent measurements of Mercury's $k_2$, it's important to remind that modeling predictions are sensitive to a wide range of highly correlated parameters. As an example, Fig. 14 shows the dependency of $h_2$ on Mercury's mantle viscosity, whose range of values is currently mainly controlled by $k_2$ estimates. For such reasons, we opt to use MCMC predictions as "guidance" to interpret our results, rather than as prior constraints to force our solution to fall within a given range.

While acknowledging these limitations, we analyze the implications of our data-driven $h_2$ estimate. The ratio of currently available $k_2 = 0.5690 \pm 0.025$ (Genova et al., 2019) with our new estimate of $h_2 = 1.55 \pm 0.65$ (taking a robust $3\sigma$ range for formal errors, or $\pm 0.45$ at $1\sigma$) yields $h_2/k_2 = 2.7 \pm 1.2$ (at $3\sigma$, or $\pm 0.9$ at $1\sigma$), which can be compared with Steinbrügge et al. (2018) to predict the size of Mercury's inner core. Even if the error associated with our solution does not allow to finely discriminate between different interior models, it constitutes a first experimental confirmation from $h_2$ of the range obtained by Genova et al. (2019), *i.e.*, a solid inner core with a radius of $590-1400$ km, marginally favoring Mercury's inner core radius to be $> 1000$ km (following the relations given in Steinbrügge et al., 2018) although this would result in a lower density, approaching the one of the outer core.

## 6 Conclusion

In this paper we presented new solutions for Mercury's rotational state based on crossover analysis of the altimetry dataset collected by MLA over the full mission (including 2 equatorial flybys in 2008 and the $2011-2015$ orbital phase). Crossover analysis has several advantages, including a lower dependence on the knowledge of small scale topography, and is a powerful tool to determine the orientation and tidal deformations of a celestial body (Mazarico et al., 2014).

In particular, we analyze the MLA crossovers "dataset" with an original procedure, including a detailed light-propagation model and optimized procedures to locate the 3-dimensional coordinates of MLA crossovers within the newly developed in-house software package PyXover. We apply an extensive error modeling based on a set of factors, as detailed in section 3.2, and VCE to ensure an optimal weighting of data and constraints to 0 applied on orbital corrections. These result in a solution based on a refined dataset and covariance information. We present the first data-based solution for Mercury's tidal Love number $h_2$, which is consistent with the presence of a solid inner core predicted by previous studies. Our results point to a complex scenario, and they highlight the great interest to improve $h_2$ and $k_2$ determination with future analysis of existing and upcoming data. Moreover, our solution for Mercury's orientation places it in a precise Cassini state, while the corresponding moment of inertia $C/MR^2$ and $C_{cm+r}/C$ are consistently computed within our solution. This results in values for the radius of the outer core that are larger than what measured by gravity (Genova et al., 2019) and consistent with other analysis based on methods sensitive to the rotation of Mercury's crust only. We interpret the apparent inconsistency between results based on gravity and "crust-related" analysis as possible evidence of different states for different layers of the planet, as discussed in section 5.

While limits posed by MESSENGER observation geometry and accuracy exist, the quality of Doppler-based orbit reconstruction can be improved by MLA contribution, as we showed crossovers to be sensitive to inconsistencies in MESSENGER orbit. While the parametrization employed in this study can only partially correct these imperfections, a combined reconstruction of MESSENGER orbits based on both Doppler and altimetry data, *e.g.*, as crossovers constraints, could potentially benefit the estimate of both orbital and empirical parameters included in the reconstruction of science orbits. In turn, such improvements would benefit the interpretation of many products and observations by the MESSENGER mission. Future observations of Mercury by the ESA mission BepiColombo (Benkhoff et al., 2010), expected to reach its orbital phase in 2025, will further constrain these parameters by extending measurements from low orbit to the Southern hemisphere of the planet. In particular, gravity estimates will profit from a less elliptical orbit and the refined X/Ka-band transponder (MORE, Iess et al., 2009) on-board the Mercury Planetary Orbiter (MPO), allowing to remove a large part of plasma noise from tracking data. The Italian Spring Accelerometer (ISA, Iafolla et al., 2010) will also contribute to a refined calibration of non-gravitational forces, *e.g.*, solar radiation pressure, acting on the spacecraft. Beside the positive impact on Mercury's gravity field estimation, these factors will likely results in an improved knowledge of its Love number $k_2$ and orientation. Altimetry measurements by the on-board BepiColombo Laser Altimeter (BELA, Thomas et al., 2007; HosseiniArani et al., 2020) could then be combined with MLA measurements to extend and refine the present analysis, either in form of crossovers or as individual measurements of surface elevation (Steinbrügge et al., 2018; Thor et al., 2020).

## Acknowledgments

S. Bertone acknowledges support by the Swiss National Science Foundation within the Advanced Postdoc Mobility grant P300P2_177776 and by NASA's Planetary Science Division Research Program through the CRESST II cooperative agreement with award number 80GSFC17M0002 (SB, SG). The MLA data were processed on the GSFC NCCS ADAPT

cluster (https://www.nccs.nasa.gov/systems/ADAPT) using the PyXover software (Bertone et al., 2020). MESSENGER orbit and attitude information used in this paper is available on the Navigation and Ancillary Information Facility (NAIF, https://naif.jpl.nasa.gov/pub/naif/pds/data/mess-e_v_h-spice-6-v1.0/messsp_1000/data/). In particular, unless differently specified, we refer to the spk/msgr_040803_150430_150430_od431sc_2.bsp orbit kernel. Other MESSENGER and Mercury's ephemeris used in this work are available on the NASA GSFC Planetary Geodynamics Data Archive (https://pgda.gsfc.nasa.gov/products/71). MLA observations are stored on the Geosciences Node of NASA's Planetary Data System (Neumann, 2018, see rdr_radr/ section).

## References


Acton, C., Bachman, N., Semenov, B., & Wright, E. (2018, jan). A look towards the future in the handling of space science mission geometry. *Planetary and Space Science*, *150*, 9–12. doi: 10.1016/j.pss.2017.02.013

Andrade, E. N. D. C. (1910, June). On the viscous flow in metals, and allied phenomena. *Proceedings of the Royal Society of London Series A*, *84*(567), 1-12. Retrieved from https://ui.adsabs.harvard.edu/abs/1910RSPSA..84....1A

Annex, A., Pearson, B., Seignovert, B., Carcich, B., Eichhorn, H., Mapel, J., ... ya Murakami, S. (2020, feb). SpiceyPy: a pythonic wrapper for the SPICE toolkit. *Journal of Open Source Software*, *5*(46), 2050. doi: 10.21105/joss.02050

Archinal, B. A., Acton, C. H., A'Hearn, M. F., Conrad, A., Consolmagno, G. J., Duxbury, T., ... Williams, I. P. (2018, February). Report of the iau working group on cartographic coordinates and rotational elements: 2015. *Celestial Mechanics and Dynamical Astronomy*, *130*(3), 22. Retrieved from https://ui.adsabs.harvard.edu/abs/2018CeMDA.130...22A doi: 10.1007/s10569-017-9805-5

Baland, R.-M., Yseboodt, M., Rivoldini, A., & Hoolst, T. V. (2017, jul). Obliquity of Mercury: Influence of the precession of the pericenter and of tides. *Icarus*, *291*, 136–159. doi: 10.1016/j.icarus.2017.03.020

Benkhoff, J., van Casteren, J., Hayakawa, H., Fujimoto, M., Laakso, H., Novara, M., ... Ziethe, R. (2010, January). BepiColombo—Comprehensive exploration of Mercury: Mission overview and science goals. , *58*(1-2), 2-20. Retrieved from `https://ui.adsabs.harvard.edu/abs/2010P\&SS...58....2B` doi: 10.1016/j.pss.2009.09.020

Bertone, S., Barker, M. K., & Mazarico, E. (2020). *PyXover - A Python Suite Of Altimetry Analysis Tools For Planetary Geodesy.* Zenodo. doi: 10.5281/ZENODO.4312137

Bierman, G. J. (1977). *Factorization methods for discrete sequential estimation* (Vol. 128). Retrieved from `https://ui.adsabs.harvard.edu/abs/1977fmds.book.....B`

Cavanaugh, J. F., Smith, J. C., Sun, X., Bartels, A. E., Ramos-Izquierdo, L., Krebs, D. J., ... Smith, D. E. (2007, August). The Mercury Laser Altimeter Instrument for the MESSENGER Mission. , *131*, 451-479. doi: 10.1007/s11214-007-9273-4

Dumberry, M. (2020, dec). The influence of a fluid core and a solid inner core on the cassini sate of mercury. *Journal of Geophysical Research: Planets*. doi: 10.1029/2020je006621

Genova, A., Goossens, S., Mazarico, E., Lemoine, F. G., Neumann, G. A., Kuang, W., ... Zuber, M. T. (2019, Apr). Geodetic Evidence That Mercury Has A Solid Inner Core. , *46*(7), 3625-3633. Retrieved from `https://ui.adsabs.harvard.edu/abs/2019GeoRL..46.3625G` doi: 10.1029/2018GL081135

Genova, A., Mazarico, E., Goossens, S., Lemoine, F. G., Neumann, G. A., Smith, D. E., & Zuber, M. T. (2018, Jan). Solar system expansion and strong equivalence principle as seen by the NASA MESSENGER mission. *Nature Communications*, *9*, 289. Retrieved from `https://ui.adsabs.harvard.edu/abs/2018NatCo...9..289G` doi: 10.1038/s41467-017-02558-1

Goossens, S., Henning, W. G., Renaud, J. P., & Genova, A. (2019, March). Constraints on models of the interior structure of mercury from measurements of its moment of inertia and tidal response. In *Lunar and planetary science conference* (p. 2203). Retrieved from `https://ui.adsabs.harvard.edu/abs/2019LPI....50.2203G`

Hansen, P. C. (1999). The l-curve and its use in the numerical treatment of inverse problems. , 119-142.

Hauck, S. A., Margot, J.-L., Solomon, S. C., Phillips, R. J., Johnson, C. L., Lemoine, F. G., ... Zuber, M. T. (2013, June). The curious case of Mercury's internal structure. *Journal of Geophysical Research (Planets)*, *118*, 1204-1220. doi: 10.1002/jgre.20091

HosseiniArani, A., Bertone, S., Arnold, D., Stark, A., Hussmann, H., Beck, T., ... Thomas, N. (2020, sep). Comprehensive in-orbit performance evaluation of the BepiColombo laser altimeter (BELA). *Planetary and Space Science*, 105088. doi: 10.1016/j.pss.2020.105088

Iafolla, V., Fiorenza, E., Lefevre, C., Morbidini, A., Nozzoli, S., Peron, R., ... Santoli, F. (2010, January). Italian spring accelerometer (isa): A fundamental support to bepicolombo radio science experiments. , *58*(1-2), 300-308. Retrieved from `https://ui.adsabs.harvard.edu/abs/2010P\&SS...58..300I` doi: 10.1016/j.pss.2009.04.005

Iess, L., Asmar, S., & Tortora, P. (2009, September). MORE: An advanced tracking experiment for the exploration of Mercury with the mission BepiColombo. *Acta Astronautica*, *65*, 666-675.

Jackson, I. (1993, may). Progress in the experimental study of seismic wave attenuation. *Annual Review of Earth and Planetary Sciences*, *21*(1), 375–406. doi: 10.1146/annurev.ea.21.050193.002111

Jorge Nocedal, S. W. (2006). *Numerical optimization.* Springer-Verlag GmbH. Retrieved from `https://www.ebook.de/de/product/5259764/jorge_nocedal_stephen_wright_numerical_optimization.html`

Knibbe, J. S., & van Westrenen, W. (2015, nov). The interior configuration of planet Mercury constrained by moment of inertia and planetary contraction. *Journal of Geophysical Research: Planets*, *120*(11), 1904–1923. doi: 10.1002/2015je004908

Konopliv, A. S., Park, R. S., & Ermakov, A. I. (2020, January). The Mercury gravity field, orientation, love number, and ephemeris from the MESSENGER radiometric tracking data. , *335*, 113386. Retrieved from `https://ui.adsabs.harvard.edu/abs/2020Icar..33513386K` doi: 10.1016/j.icarus.2019.07.020

Kreslavsky, M. A., Head, J. W., Neumann, G. A., Zuber, M. T., & Smith, D. E. (2014, December). Kilometer-scale topographic roughness of mercury: Correlation with geologic features and units. , *41*(23), 8245-8251. Retrieved from https://ui.adsabs.harvard.edu/abs/2014GeoRL..41.8245K doi: 10.1002/2014GL062162

Kusche, J. (2003). Noise variance estimation and optimal weight determination for goce gravity recovery. *Advances in Geosciences*, *1*, 81–85. Retrieved from http://www.adv-geosci.net/1/81/2003/ doi: 10.5194/adgeo-1-81-2003

Lemoine, F. G., Goossens, S., Sabaka, T. J., Nicholas, J. B., Mazarico, E., Rowlands, D. D., . . . Zuber, M. T. (2013, August). High-degree gravity models from grail primary mission data. *Journal of Geophysical Research (Planets)*, *118*, 1676-1698. doi: 10.1002/jgre.20118

Margot, J.-L. (2009, Dec). A Mercury orientation model including non-zero obliquity and librations. *Celestial Mechanics and Dynamical Astronomy*, *105*(4), 329-336. Retrieved from https://ui.adsabs.harvard.edu/abs/2009CeMDA.105..329M doi: 10.1007/s10569-009-9234-1

Margot, J.-L., Hauck, I. I., Steven A., Mazarico, E., Padovan, S., & Peale, S. J. (2018, June). Mercury's internal structure. *arXiv e-prints*, arXiv:1806.02024. Retrieved from https://ui.adsabs.harvard.edu/abs/2018arXiv180602024M

Margot, J.-L., Peale, S. J., Solomon, S. C., Hauck, I. I., Steven A., Ghigo, F. D., Jurgens, R. F., . . . Campbell, D. B. (2012, October). Mercury's moment of inertia from spin and gravity data. *Journal of Geophysical Research (Planets)*, *117*, E00L09. Retrieved from https://ui.adsabs.harvard.edu/abs/2012JGRE..117.0L09M doi: 10.1029/2012JE004161

Mazarico, E., Barker, M. K., Neumann, G. A., Zuber, M. T., & Smith, D. E. (2014, Apr). Detection of the lunar body tide by the lunar orbiter laser altimeter. , *41*(7), 2282-2288. Retrieved from https://ui.adsabs.harvard.edu/abs/2014GeoRL..41.2282M doi: 10.1002/2013GL059085

Mazarico, E., Genova, A., Neumann, G. A., Smith, D. E., & Zuber, M. T. (2015, May). Simulated recovery of Europa's global shape and tidal Love numbers from altimetry and radio tracking during a dedicated flyby tour. , *42*, 3166-3173. doi: 10.1002/2015GL063224

Neumann, G. (2018). *MESSENGER MLA Derived (GDR/RADR) Data Bundle.* Geosciences Node. doi: 10.17189/1518575

Peale, S. J. (1988). The rotational dynamics of mercury and the state of its core. In F. Vilas, C. R. Chapman, & M. S. Matthews (Eds.), *Mercury, university of arizona press* (p. 461-493). Retrieved from `https://ui.adsabs.harvard.edu/abs/1988merc.book..461P`

Peale, S. J., Phillips, R. J., Solomon, S. C., Smith, D. E., & Zuber, M. T. (2002, sep). A procedure for determining the nature of mercury's core. *Meteoritics & Planetary Science*, *37*(9), 1269–1283. doi: 10.1111/j.1945-5100.2002.tb00895.x

Phillips, R. J., Byrne, P. K., James, P. B., Mazarico, E., Neumann, G. A., & Perry, M. E. (2018). Mercury's Crust and Lithosphere: Structure and Mechanics. In *Mercury: The view after messenger* (p. 52–84). Cambridge University Press. doi: 10.1017/9781316650684.004

Rosat, S., Rosenblatt, P., Trinh, A., & Dehant, V. (2008, dec). Mars and mercury rotation variations from altimetry crossover data: Feasibility study. *Journal of Geophysical Research*, *113*(E12). doi: 10.1029/2008je003233

Rowlands, D. D., Pavlis, D. E., Lemoine, F. G., Neumann, G. A., & Luthcke, S. B. (1999). The use of laser altimetry in the orbit and attitude determination of Mars Global Surveyor. , *26*, 1191-1194. doi: 10.1029/1999GL900223

Soffel, M., Klioner, S. A., Petit, G., Wolf, P., Kopeikin, S. M., Bretagnon, P., … Xu, C. (2003, December). The iau 2000 resolutions for astrometry, celestial mechanics, and metrology in the relativistic framework: Explanatory supplement. , *126*(6), 2687-2706. Retrieved from `https://ui.adsabs.harvard.edu/abs/2003AJ....126.2687S` doi: 10.1086/378162

Sohl, F., & Spohn, T. (1997, jan). The interior structure of Mars: Implications from SNC meteorites. *Journal of Geophysical Research: Planets*, *102*(E1), 1613–1635. doi: 10.1029/96je03419

Solomon, S. C., McNutt, R. L., Watters, T. R., Lawrence, D. J., Feldman, W. C., Head, J. W., … Zuber, M. T. (2008, July). Return to Mercury: A Global Perspective on MESSENGER's First Mercury Flyby. *Science*, *321*, 59. doi: 10.1126/science.1159706

Stark, A., Oberst, J., Preusker, F., Gwinner, K., Peale, S. J., Margot, J.-L., … Solomon, S. C. (2015, November). Mercury's rotational parameters from MESSENGER image and laser altimeter data: A feasibility study. , *117*, 64-72. doi:

10.1016/j.pss.2015.05.006

Stark, A., Oberst, J., Preusker, F., Peale, S. J., Margot, J.-L., Phillips, R. J., ... Solomon, S. C. (2015, October). First MESSENGER orbital observations of Mercury's librations. , *42*(19), 7881-7889. Retrieved from `https://ui.adsabs.harvard.edu/abs/2015GeoRL..42.7881S` doi: 10.1002/2015GL065152

Steinbrügge, G., Stark, A., Hussmann, H., Wickhusen, K., & Oberst, J. (2018, September). The performance of the BepiColombo Laser Altimeter (BELA) prior launch and prospects for Mercury orbit operations. , *159*, 84-92. Retrieved from `https://ui.adsabs.harvard.edu/abs/2018P\&SS..159...84S` doi: 10.1016/j.pss.2018.04.017

Steinbrügge, G., Dumberry, M., Rivoldini, A., Schubert, G., Cao, H., Schroeder, D. M., & Soderlund, K. (2020, dec). Challenges on mercury's interior structure posed by the new measurements of its obliquity and tides. *Geophysical Research Letters*. doi: 10.1029/2020gl089895

Steinbrügge, G., Padovan, S., Hussmann, H., Steinke, T., Stark, A., & Oberst, J. (2018, oct). Viscoelastic Tides of Mercury and the Determination of its Inner Core Size. *Journal of Geophysical Research: Planets*, *123*(10), 2760–2772. doi: 10.1029/2018je005569

Susorney, H. C. M., Barnouin, O. S., Ernst, C. M., & Byrne, P. K. (2017, June). The surface roughness of mercury from the mercury laser altimeter: Investigating the effects of volcanism, tectonism, and impact cratering. *Journal of Geophysical Research (Planets)*, *122*(6), 1372-1390. Retrieved from `https://ui.adsabs.harvard.edu/abs/2017JGRE..122.1372S` doi: 10.1002/2016JE005228

Thomas, N., Spohn, T., Barriot, J.-P., Benz, W., Beutler, G., Christensen, U., ... Whitby, J. (2007, July). The BepiColombo Laser Altimeter (BELA): Concept and baseline design. , *55*, 1398-1413. doi: 10.1016/j.pss.2007.03.003

Thor, R. N., Kallenbach, R., Christensen, U. R., Stark, A., Steinbrügge, G., Ruscio, A. D., ... Oberst, J. (2020, jan). Prospects for measuring mercury's tidal love number h2 with the BepiColombo laser altimeter. *Astronomy & Astrophysics*, *633*, A85. doi: 10.1051/0004-6361/201936517

Tikhonov, A. N., Leonov, A. S., & Yagola, A. G. (1998). *Nonlinear ill-posed prob-*

*lems* (Vol. 14). Retrieved from https://ui.adsabs.harvard.edu/abs/1998nipp.book.....T

Van Hoolst, T., & Jacobs, C. (2003, November). Mercury's tides and interior structure. *Journal of Geophysical Research (Planets)*, *108*(E11), 5121. Retrieved from https://ui.adsabs.harvard.edu/abs/2003JGRE..108.5121V doi: 10.1029/2003JE002126

Verma, A. K., & Margot, J.-L. (2016, September). Mercury's gravity, tides, and spin from MESSENGER radio science data. *Journal of Geophysical Research (Planets)*, *121*, 1627-1640. doi: 10.1002/2016JE005037

Virtanen, P., , Gommers, R., Oliphant, T. E., Haberland, M., Reddy, T., ... van Mulbregt, P. (2020, feb). SciPy 1.0: fundamental algorithms for scientific computing in python. *Nature Methods*, *17*(3), 261–272. doi: 10.1038/s41592-019-0686-2

Zuber, M. T., Smith, D. E., Phillips, R. J., Solomon, S. C., Neumann, G. A., Hauck, S. A., ... Yang, D. (2012, mar). Topography of the northern hemisphere of mercury from MESSENGER laser altimetry. *Science*, *336*(6078), 217–220. doi: 10.1126/science.1218805